Harnessing Conformational Disorder of Organic Cations for Efficient Blue Quasi-2D Perovskite LEDs

Lyuchao Zhuang†[1,2], Chuanzhao Li†[1], Qi Wei†[1], Renlong Zhu[3], Hui Ren[1], Fangyi Shi[1], Kai Leng[1], Mingjie Li[1,2], Shuji Ye*[3], Shu Ping Lau*[1,2]*

[1]Department of Applied Physics, The Hong Kong Polytechnic University, Hung Hum, Kowloon, Hong Kong SAR, China.

[2]Photonic Research Institute, The Hong Kong Polytechnic University, Hung Hum, Kowloon, Hong Kong SAR, China.

[3] Hefei National Research Center for Physical Sciences at the Microscale, University of Science and Technology of China, Hefei, Anhui 230026, China.

† These authors contributed equally to this work.

*Corresponding author: ming-jie.li@polyu.edu.hk (M.L.), shujiye@ustc.edu.cn (S.Y.), apsplau@polyu.edu.hk (S.P.L.).

Abstract

Despite quasi-2D perovskite offering great control over the optoelectronic properties, disordered organic cations are often perceived as detrimental to device performance, primarily affecting charge carrier mobility. However, we propose that such disordered organic cations-enabled excellent excitonic properties can be beneficial for fabricating high-efficiency perovskite light-emitting diodes (PeLEDs) facilitated by reduced dielectric screening effect. Here, by incorporating acetamidinium bromide (AABr) additives, we precisely manipulate and meticulously probe the conformational disorder of organic cation using sum frequency generation vibrational spectroscopy (SFG-VS). Finally, we elucidate a distinctive inverse relationship between the degree of conformational order, characterized as relative structure ordering (RSO), and key performance metrics such as photoluminescence quantum yield (PLQY) and external quantum efficiency (EQE). By optimizing the configurational disorder, sky-blue (485 nm) PeLEDs achieve a noteworthy EQE of 14.42% and exhibit significantly prolonged operational stability in open-air conditions. This finding underscores the potential advantages of disordered organic cations in enhancing exciton properties and radiative recombination efficiency.

Introduction

Quasi-2D perovskites have attracted much interest for their use in next-generation photovoltaic devices and light sources due to their superior environmental stability, excellent optoelectronic properties with remarkable tunability, and reduced ion migration[1-4]. In general, quasi-2D perovskites have the chemical formula $(A)_2A'_{n-1}M_nX_{3n+1}$, where A represents bulky organic ammonium and A', M, and X are a small organic or alkaline metal cation, a group IV metal, and a halogen, respectively. Due to the natural ion character of the perovskite lattice, chemical tuning of the organic cations is a promising strategy to obtain high-performance devices. Understanding the organic cations conformational and their effects associated with optoelectronic properties is of fundamental importance; however, it remains an unsolved problem in the perovskite light-emitting diodes (PeLEDs) field.

Previous studies have shown that the conformational disorder of organic cations always considerably deteriorates the charge carrier mobility and free carrier diffusion length[5-7], hampering the high-power conversion efficiency (PCE) of perovskite solar cells (PSCs). Compared to PSCs, the efficiency of quasi-2D PeLEDs is positively related to their exciton properties, including exciton binding energy (E_b) and photoluminescence quantum yield (PLQY) [8]. It is well acknowledged that excitonic behavior and free charge carrier transport compete with each other [7, 9]. Consequently, leveraging the conformational disorder of organic cations is anticipated to enhance the excitonic behavior of perovskites, albeit at the expense of compromising the charge carrier transport properties. The excellent charge carrier transport properties are not the prerequisite of high-performance PeLED devices because the thickness of the PeLED device (~100 nm) is much thinner than that of PSCs (~1 μm)[10]. The carrier spatial confinement can be an advantage in light-emitting applications owing to enhanced E_b, and decreased nonradiative recombination caused by deep-level traps at the surface and grain boundary of the perovskite film[5, 11]. The conformational disorder of organic cations thus holds the potential to bestow perovskite films with higher PLQY and E_b,

along with strong charge carrier spatial confinement, rendering them suitable for PeLED devices.

To materialize this idea, we tailor the molecular disorder of conjugated organic cations phenethylammonium (PEA^+) using acetamidinium bromide (AABr) as an additive due to the molecular interactions between PEA^+ and AA^+. Theoretically, the weak crystallinity of organic cations severely restricts the range of experimental techniques for determining their stacking and orientation in quasi-2D perovskite films[6, 7]. To precisely identify the conformational disorder of organic cations, in this study, we employed advanced symmetry-sensitive sum frequency generation vibrational spectroscopy (SFG-VS) to detect the molecular disorder of organic cations among quasi-2D layered perovskites and investigate its impact on the exciton properties and emission performance of devices. As expected, the inverse dependence of the PLQY and external quantum efficiency (EQE) on the relative structure ordering (RSO) of the phenyl ring is observed in this study, indicating that the disordered conformation of conjugated organic cations can enhance the exciton properties and radiative recombination efficiency. It is suggested that the primarily ignored molecular stacking leads to an increased mismatch of dielectric constants between the organic layer and inorganic framework, resulting in an enhanced E_b. Moreover, notably, the deteriorated charge transfer in the disordered systems allows energy transfer with high efficiencies. Together, these synergetic effects led to highly efficient PeLEDs with an EQE of 14.42%. Our findings highlight the importance of a molecular-level understanding of the stacking arrangement of organic cations in quasi-2D perovskites to modulate the optoelectronic properties.

Results

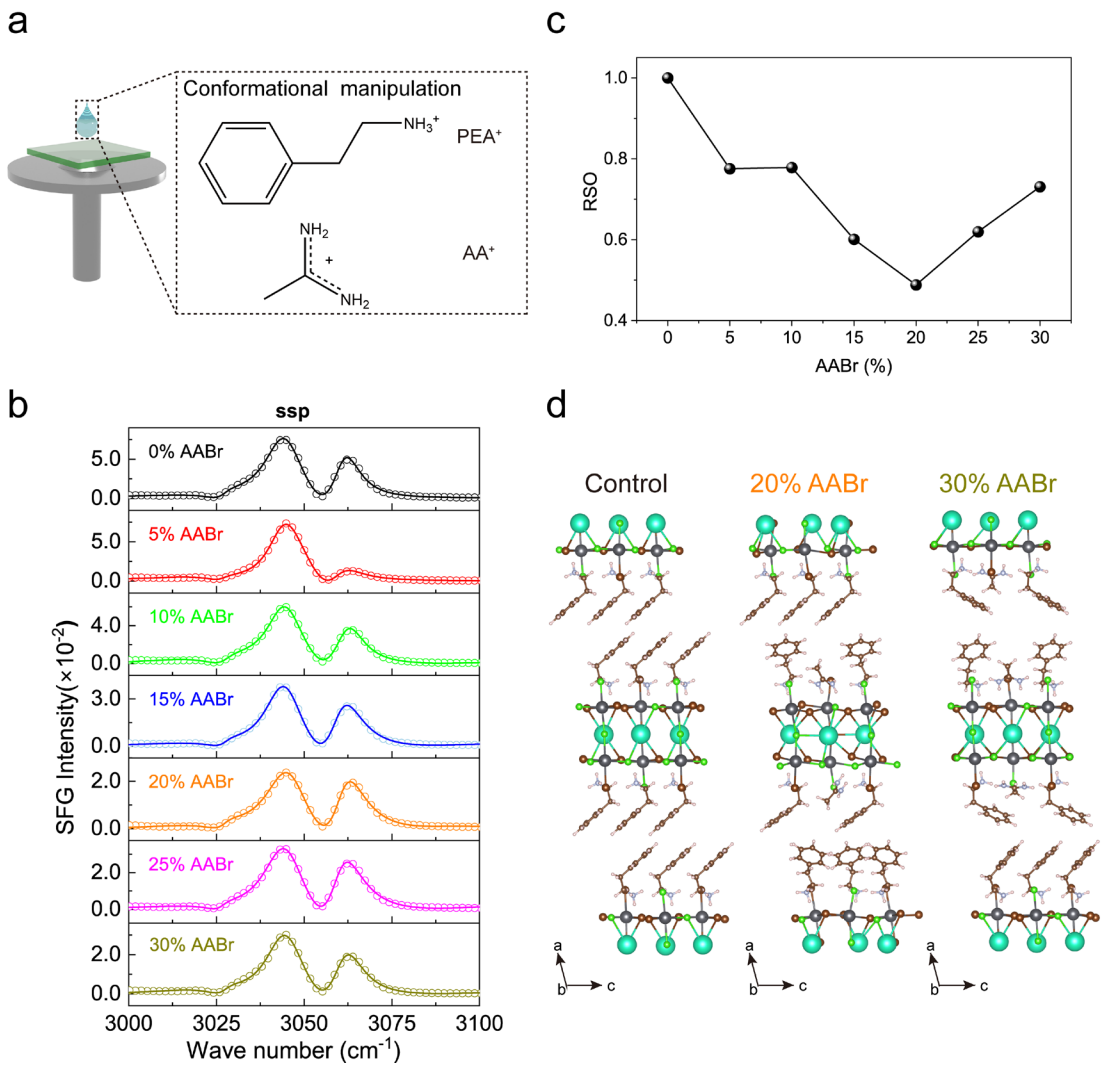

Figure 1. Conformational disorder control. (a) Schematic of the quasi-2D perovskite film preparation approach. (b) ssp-polarized SFG spectra of quasi-2D perovskite with AABr varying from 0% - 30%, where scatter symbols represent experimental data, and the solid lines are fitted results. (c) The relative structural ordering (RSO) of the phenyl group derived from SFG spectra. (d) The crystal structures of the n = 2 2D perovskite for the control, 20% AABr and 30% AABr samples.

We prepared perovskite emissive layers from precursors with a stoichiometry of $CsBr:PbBr_2:PbCl_2:PEABr:AABr$ = 1: 0.6: 0.4: 1: x (x = 0% - 30%), where AABr is acetamidinium bromide (Methods) (Figure 1a, Figure S1). Owing to the unique structural tolerance of the 2D perovskite and the nature of the organic spacer, it allows a variety of stacking arrangements within the rather rigid inorganic $[PbBr_6]^{4-}$ cluster.

X-ray diffraction (XRD) was used to investigate the crystal structure of the quasi-2D perovskite films, as shown in Figure S2. The diffraction peak at 3.7° indicates that n = 2 quasi-2D perovskite coexists in the as-prepared perovskite films[12]. To further confirm the existence of AABr in the decorated films, X-ray photoelectron spectroscopy (XPS) measurements were performed. The XPS results show that the N 1s spectra of the perovskite films can be deconvoluted into two contributions from PEA^+ at 402.1 eV and AA^+ at 400.7 eV (Figure S3). A shift to higher binding energy in the N 1s spectra for PEA^+ of 20% AABr compared to that of the control can be observed, from 401.7 eV to 402.1 eV, suggesting a strong molecular interaction between PEA^+ and AA^+ cations[13]. AA^+ and PEA^+ coexist in the organic layer and may introduce two competing effects: steric hindrance and π-π interactions. During the fast crystallization process, the interaction of organic cations contributes to the random packing arrangement; for example, rotating around the axis with the NH_3^+ as the center leads to orientation disorder inevitably. We assume that the π-π interaction plays a predominant role that disturbs the ordered stacking of PEA^+ when the concentration is low, whereas steric hindrance takes over the conformation distribution as the concentration further increases, gradually reversing the structural disorder by limiting the PEA^+ group rotation. Therefore, varying the concentration of AABr can easily control the conformation distribution of PEA^+ conjugated organic cations.

Consequently, choosing the appropriate content of AABr is crucial to tailoring the conformational order of PEA^+ in the perovskite film. To verify this conjecture, we first examined the conformational information of PEA^+ with different concentrations of AABr using SFG-VS. As a second-order nonlinear optical technique, SFG-VS is a powerful tool for evaluating molecular symmetry, orientation, and orientational disorder. SFG-VS has been used to probe the molecular orientation of the organic cations of lead-halide perovskites[14-16] and the passivator layer capping above the perovskite interface[17, 18].

Figure 1b displays the ssp spectra of the phenyl groups of quasi-2D perovskites prepared with different concentrations of AABr. The SFG spectra show two strong resonant peaks at ~3044 cm^{-1} and ~3061 cm^{-1}. The ppp spectra are provided in Figure

S4a. According to previous studies, the SFG spectra of the C-H aromatic stretches of phenyl groups have five vibrational modes ranging from 3000 to 3100 cm^{-1}, which are both infrared and Raman active[19]. The resonance frequencies of these five modes appear at ~3027, ~3044, ~3055, ~3061, and ~3090 cm^{-1}, which are attributed to the v_{20b}, v_{7a}, v_{7b}, v_2, and v_{20a} vibrational modes, respectively[19-23]. Therefore, the observed ~3044 cm^{-1} and ~3061 cm^{-1} peaks arise from the v_{7a} and v_2 vibrational modes, respectively. To quantitatively analyze the intensity dependence on different ratios of AABr in quasi-2D perovskite, we fitted the spectra following a standard procedure (note 1). In principle, a chemical group's orientation tilt angle (θ) can be determined by relating the second-order susceptibility $\chi_{ijk}^{(2)}\left(i,j,k=x,y,z\right)$ to the molecular hyperpolarizability $\beta_{lmn}\left(l,m,n=a,b,c\right)$[24, 25]. Many studies have reported the analysis of the orientation of the phenyl group[26-28]. We used the v_2 vibration mode (~3061 cm^{-1}) to determine the orientation (see note 2). According to the literature[29], the hyperpolarizability ratio $R=\beta_{ccc}/\beta_{aac}$ for the v_2 vibration mode equals 1.13 by density function theory calculation. The measured $\chi_{ppp}^{(2)}/\chi_{ssp}^{(2)}$ ratio of the ~3061 cm^{-1} peak is illustrated in Figure S4b. The resulting relation between the $\chi_{ppp}^{(2)}/\chi_{ssp}^{(2)}$ ratio and the tilt angle of the phenyl group (θ_{phenyl}) is presented in Figure S4c. With the assumption of a δ-distribution, the tilt angle of θ_{phenyl} is deduced based on the measured $\chi_{ppp}^{(2)}/\chi_{ssp}^{(2)}$ ratio of the ~3061 cm^{-1} peak. The tilt angles of θ_{phenyl} are determined to be 32.9°, 50.6°, 25.1°, 23.2°, 20.2°, 21.5°, and 34.5° for quasi-2D perovskites with 0, 5, 10, 15, 20, 25, and 30% AABr, respectively (Figure S4d).

With the knowledge of the orientational information, we estimated the structure ordering by the effective molecular number $\left(\langle N\rangle\right)$ contributing to SFG signals[7]. The relative structure ordering (*RSO*) (relative to the control sample (0% AABr)) is then defined with the variation of the orientation angle (see note 3). The *RSO* initially decreases and then increases as the compositional content of the AABr increases (Figure 1c), as we predicted previously. The minimum *RSO* is found when the AABr

concentration is 20%. Consequently, we can control the amount of AABr to harness conformation disorder, as shown in Figure 1d.

The different packing arrangements and orientational disorder of the spacer cations generally result in macroscopic differences in optoelectrical properties. For instance, molecular packing inside the organic layers contributes to higher crystal rigidity, reducing electron-phonon interactions and thus achieving high luminescence efficiency[30]. Furthermore, quasi-2D perovskite is a strongly quantum-confined system in which the exciton binding energy (E_b) is determined by the dielectric constants of the inorganic frameworks (ε_w) and the organic cations (ε_b)[31, 32].

The stacking arrangement of spacer cations has been confirmed by SFG-VS, driven by the strong interlayer molecular interaction[13, 33, 34]. We suspect E_b is additionally strengthened by the discrepancy in dielectric constants between the inorganic framework and the organic layer, resulting from conformational disorder[35, 36]. Theoretically, the correlation among E_b of 2D and 3D excitons and the dielectric constant of media is expressed by the following equation[37]:

$$E_b^{2D} = 4\left(\frac{\varepsilon_w}{\varepsilon_b}\right)^2 E_b^{3D}$$

where ε_w and ε_b are the dielectric constants of the inorganic frameworks and the organic cations, respectively. E_b^{3D} stands for the exciton binding energy of the corresponding 3D perovskite. The increase in ε_w and/or the decrease in ε_b would lead to an increase in E_b of the quasi-2D perovskite. We performed density functional theory (DFT) simulations on n = 2 quasi-2D perovskites to verify that the photophysical properties are associated with the dielectric confinement effect. Details of the computational methodology are elaborated in note 4. The calculated dielectric constants for the organic and inorganic parts of the 0%, 20% and 30% AABr samples along the three polarization directions are shown in Figure S5. According to the DFT calculation, such distinct organic layer stacking for the 20% AABr sample would lead to a higher $\varepsilon_w/\varepsilon_b$ value[32]. The schematic representations of the predicted dielectric constants for the control, 20% AABr, and 30% AABr samples are summarized in Figure 2a. Interestingly, the calculated $\varepsilon_w/\varepsilon_b$ values seemed to increase with respect to the conformational disorder,

following the order 20% AABr > 30% AABr > Control, as shown in Table S1. The $\varepsilon_w/\varepsilon_b$ value was 4.13 for the 20% AABr sample. Thus, it is believed that this approach leads to an increase in dielectric contrast between the $[PbX_6]^{4-}$ halide layer and the intercalating ammonium cation, which would increase the E_b, hence improving the emission quantum efficiency. As a result, it is recognized that the unique intermolecular packing of spacer cations introduces different mismatch dielectric constants, resulting in E_b evolution[32].

To understand the variation trend of E_b precisely, we conducted temperature-dependent PL measurements to determine the E_b for quasi-2D perovskite films quantitatively, as displayed in Figure 2b and Figure S6. The extracted E_b of the control and 20% AABr samples for high-n phases (n > 3) are estimated to be 88.5 meV and 107.4 meV, respectively (Figure 2d) (note 5). In contrast, E_b decreases as the AABr concentration continuously increases, as shown in Figure S7. The combination of experimental and theoretical approaches thus demonstrates that the optoelectronic properties of quasi-2D perovskites can be harnessed through modulation of dielectric confinement caused by the stacking disorder of organic molecules.

Additionally, the PLQY is positively associated with E_b, which can be fine-tuned by the quantum confinement effect[8, 35]. To verify this speculation, we recorded the PL properties as a function of AABr concentration. As displayed in Figure S8, the control perovskite film exhibits a sky-blue emission at 490 nm, while a blueshift can be observed with increased AABr concentration. Indeed, the photoluminescence quantum yield (PLQY) of the perovskite film with the optimized ratio of 20% AABr is improved by 4.5-fold to 80.29% compared to that of the control samples (Figure 2c). Then, we demonstrate the dependence of the PLQY derived from quasi-2D perovskites with various AABr concentrations on *RSO*, as shown in Figure 2d. As expected, this correlation implies that the conformational disorder of organic cations is the structural origin of radiative recombination facilitation in these quasi-2D perovskite films. In principle, the large enhancement of the PLQY can also be attributed to a significantly elongated PL lifetime[38]. Time-resolved PL (TRPL) measurements were also conducted to study the exciton dynamics in perovskite films (Figure S9). The TRPL curves are

fitted using triexponential decay functions, and the fitting parameters are summarized in Table S2. The average lifetime improves notably with increasing AABr concentration. The spatial limitation of the exciton, benefiting from the conformational disorder, facilitates radiative recombination rather than annihilation at defects of the grain boundary or surface.

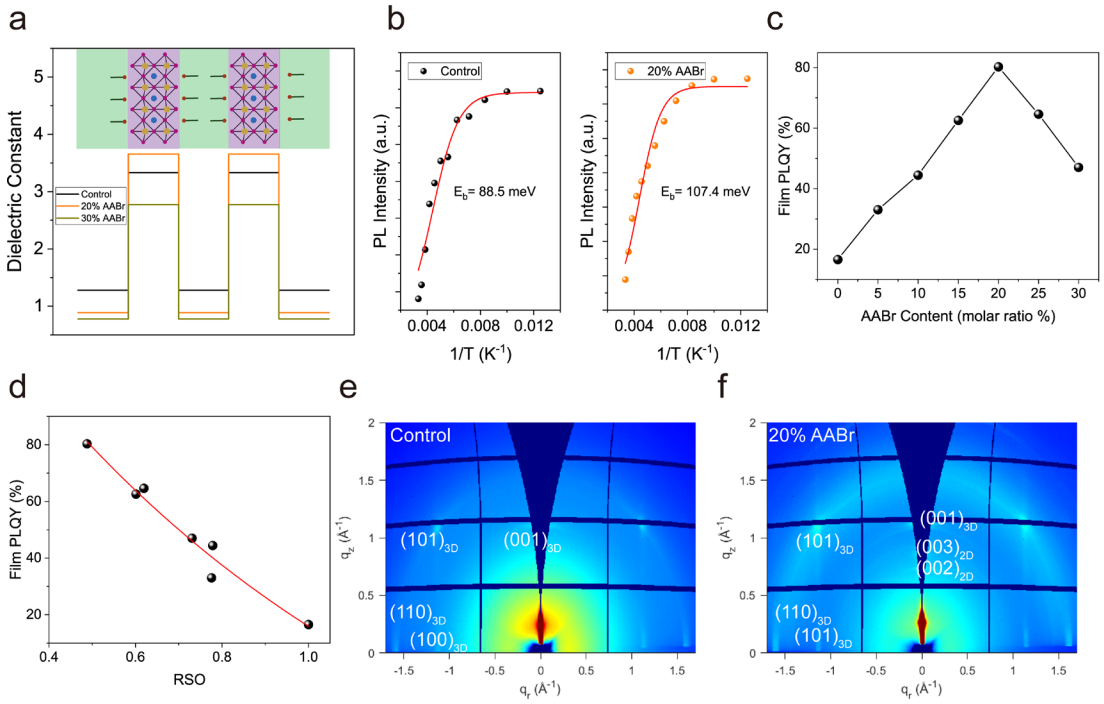

Figure 2. Dielectric constant calculation and optical properties. (a) Calculated dielectric profiles of the control, 20% AABr and 30% AABr quasi-2D perovskites. The upper figure illustrates the crystal structure of the n = 2 quasi-2D perovskite, where the green and purple regions represent the barrier and quantum well regions, respectively. (b) Integrated PL intensity and derived E_b of the control and 20% AABr quasi-2D perovskite films as a function of reciprocal temperature. (c) Photoluminescence quantum yield (PLQY) of quasi-2D perovskite films with different amounts of AABr added. (d) Dependence of the PLQY values derived from quasi-2D perovskites with various AABr concentrations on RSO. GIWAXS patterns of (e) control and (f) 20% AABr quasi-2D perovskite films.

Some studies have revealed that the optoelectronic properties of perovskites are strictly linked to the crystal orientation[39, 40]. Therefore, to elucidate the effect of the inorganic $[PbBr_6]^{4-}$ slab orientation, we further performed Grazing-Incidence Wide-Angle X-ray Scattering (GIWAXS) measurements of the control and AABr-incorporated quasi-2D perovskites to collect more information on crystal orientation (Figure 2e, f and Figure

S10). Debye–Scherrer rings indicate a random crystalline orientation in the as-synthesized quasi-2D perovskite films[41]. Moreover, the *q* and 2θ curves related to the diffraction intensity of the perovskite films and the azimuthally integrated curves extracted from GIWAXS also provide intuitive evidence of higher crystallinity and non-preferential crystal orientation after AABr addition (Figure S11, S12). Based on the similar crystal orientation given by the results of GIWAXS, we conclude that the difference in the packing arrangement of the organic cations would lead to the different optoelectronic properties of perovskite films.

For the natural MQWs structure, the insulating organic layers are believed to hinder interlayer charge transfer, allowing energy transfer to occur with high efficiencies. Such correlated dynamics are consistent with the conformation of organic cations. To determine the photophysical processes, we performed transient absorption spectroscopy (TA). As illustrated in Figure S13, the excitonic absorption peaks can be clearly identified for low-*n* phases from UV-Vis absorption. In detail, distinctive ground-state bleach (GSB) peaks at ~ 421, ~ 448, and 481 nm are identified for the control sample, corresponding to the $n = 2$, $n = 3$, and $n \geq 4$ phases, respectively (Figure 3a). Apparently, the 20% AABr perovskite thin films also feature pronounced GSB peaks corresponding to the $n = 2$, $n = 3$, and $n \geq 4$ phases (Figure 3b). We suspect that the $n = 2$ $(PEA_xAA_{1-x})_2CsPb_2(Br_{0.6}Cl_{0.4})_7$ phases can be divided into PEA-rich and AABr-rich phases. Since their lattice space has no difference, it is difficult to distinguish them from the XRD. Based on the UV-Vis spectra, we observe that with the increase of AABr, the 430 nm GSB will increase gradually. Thus, we tend to assign the 430 nm GSB to the AABr-rich $n = 2$ phases $(PEA_xAA_{1-x})_2CsPb_2(Br_{0.6}Cl_{0.4})_7$. We further estimated the contribution of each domain, as shown in Figure S14. The adoption of AABr almost does not change the phase proportion of $n \geq 4$ phases when the AABr concentration is below 20%, whereas the high-*n* phases decrease when the concentration further increases to 30%. The distinct decay kinetics of each GSB is extracted and shown in Figure 3c, d. The fitting parameters are listed in Table S3. The fast component of low-n phases can be attributed to an energy transfer from the small-*n* to the large-*n* phases, while the slow component belongs to the charge-trapping

process[43, 44]. Notably, the decay kinetics for high-*n* phases of 20% AABr perovskite film show a shorter formation time of 0.34 ps, which is almost half of the formation time for the control sample (0.62 ps). Consequently, an accelerated and more efficient exciton energy transfer is confirmed inside the 20% sample with the lowest *RSO* [45, 46], enabling more efficient radiative recombination.

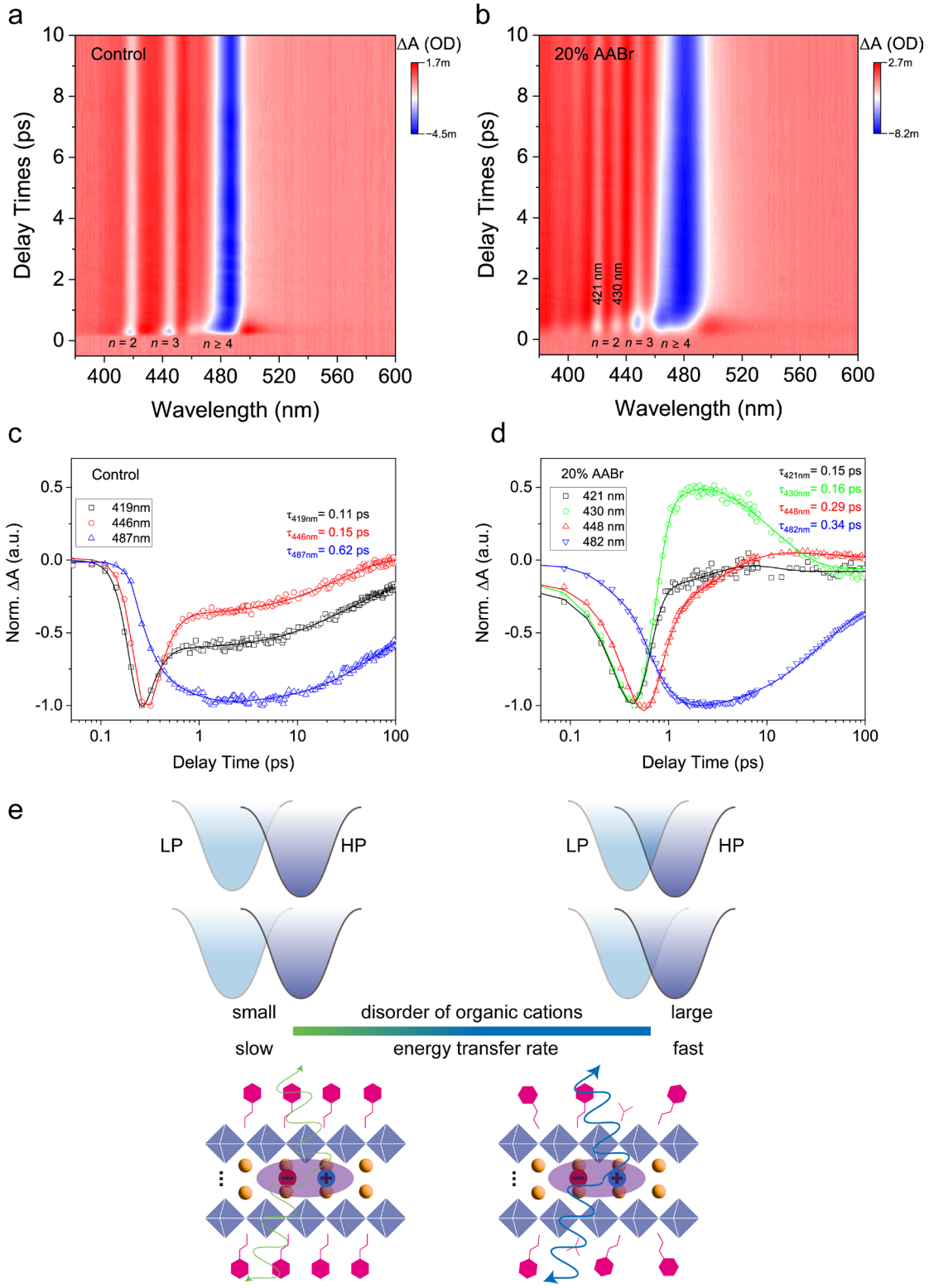

Figure 3. Energy transfer in quasi-2D perovskite films. Time-wavelength-dependent TA color map for the control (a) and 20% AABr (b) perovskite films. TA spectra at selected time scales and carrier dynamics probed at different wavelengths for the control (c) and 20% AABr (d) perovskite films. (e)

Schematics of energy transfer rate for the control and 20% AABr quasi-2D perovskite thin films, LP – low-*n* phases, HP – high-*n* phases.

As illustrated in Figure 3e, the energy transfer rate is directly affected by the steric properties of the organic cation. The conformation disorder or length of organic spacer plays a critical role in the donor-acceptor distance and dielectric effect, both of which are believed to be of importance to energy transfer rate[47-49]. According to the XRD results, we can determine that the interlayer distance of QMWs is very similar (Figure S2). Therefore, we can conclude that the conformational disorder of organic cations exhibited a disordered dipole moment direction, thus providing species with lower polarization and dipole dielectric response so that no strengthened dielectric screening effect appeared. It further deteriorates the charge transfer, whereas realizing effective energy transfer to the recombination center produces a high-efficiency blue emission.

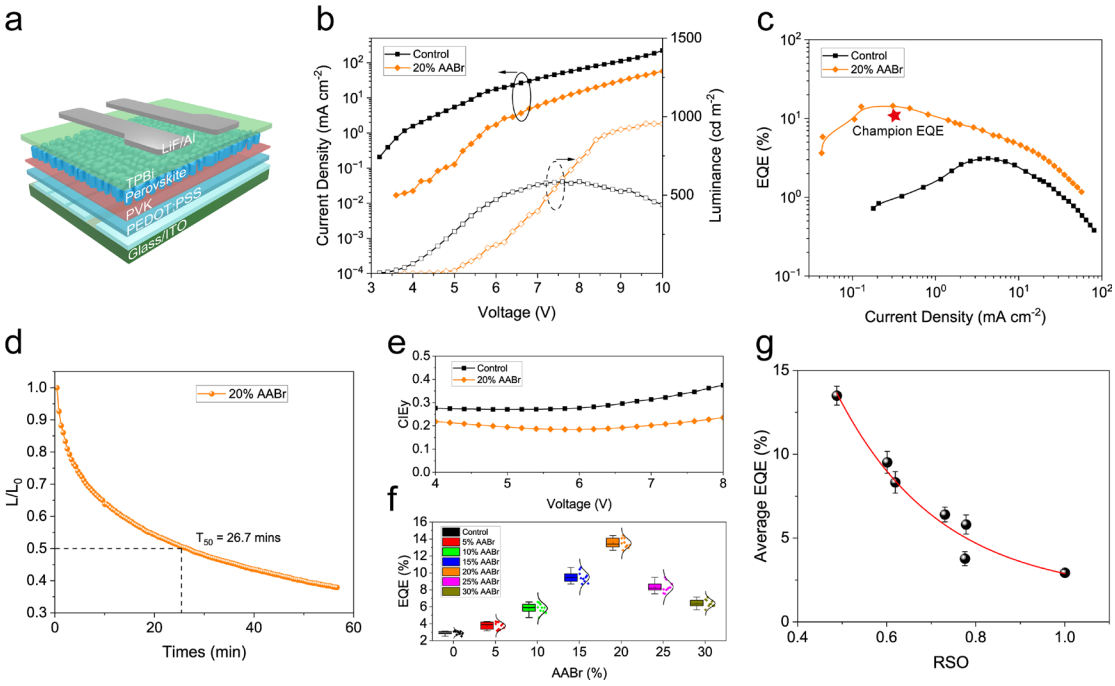

Figure 4. Device architecture and performance of blue PeLEDs. (a) PeLED architecture. J-V-L curves (b) and EQE-J (c) for control and 20% AABr quasi-2D PeLEDs. (d) Operating stability of 20% AABr quasi-2D PeLEDs. (e) Spectral stability for control and 20% AABr quasi-2D PeLEDs. Representative plots of CIEy versus applied voltage. (f) EQE distribution with the AABr concentration varying from 0% - 30%. (g) Dependence of the average peak EQE values derived from quasi-2D perovskites with various AABr concentrations on RSO.

Considering the exceptional emissive properties of quasi-2D perovskite films, which are crucial for achieving high-performance PeLED devices, it is reasonable to anticipate that perovskite films with conformation disorder are promising for electroluminescence (EL) enhancement, based on the above observations. To evaluate the device performance, PeLEDs were fabricated with the structure of indium tin oxide (ITO)/PEDOT:PSS/poly(9-vinylcarbazole) (PVK)/perovskite/2,2′,2″-(1,3,5-benzinetriyl)tris(1-phenyl-1H-benzimidazole) (TPBi)/lithium fluoride (LiF)/aluminum, as depicted in Figure 4a. Scanning electron microscopy (SEM) and atomic force microscopy (AFM) measurements were conducted to investigate the morphology evolution of perovskite films. Figures S15 and 16 illustrate that the top-view SEM and AFM images exhibit uniform and dense films without observable pinholes for AABr-treated samples, suggesting the potential for high-quality optoelectronic device construction. The current density-voltage (J-V) curves of PeLEDs indicate that the current leakage at lower bias is reduced (Figure 4b). Such a phenomenon is ascribed to the suppression of perovskite defects[50]. The control devices exhibit low performance with 3.11% EQE and display a noticeable brightness roll-off under high bias voltage, indicating that strong nonradiative recombination occurs[51]. Notably, when comparing the devices processed with various AABr concentrations, we observe that the 20% AABr-treated device delivery considerably enhanced the EQE of 14.42%, accompanied by decent reproducibility with an average peak EQE of 13.50% (Figure 4c, Figure S17).

The employment of AABr facilitates hole injection due to a reduced hole injection barrier[52], which also accounts for the improved PeLED performance (Figure S18). Furthermore, we record the operation stability of the PeLEDs under continuous operation with an initial luminance of approximately 100 cd m^{-2} to evaluate their lifetime. The half-lifetime (T_{50}) for 20% AABr PeLEDs was determined to be 26.7 min (Figure 4d) with encapsulation under ambient atmosphere. Importantly, we also tracked the evolution of the EL spectra at different applied voltages. The EL spectrum can stabilize at 485 nm with increasing driven bias (Figure 4e, Figure S19), indicating suppressed halide ion migration under electrical stimulation.

Nevertheless, the control devices undergo distinct emission color changes induced by halide migration as the bias voltage increases[53, 54]. We tend to attribute the improved lifetime to the suppression of ion migration resulting from the low defect density[55-57]. To support this hypothesis, we used space-charge-limited current (SCLC) measurements to determine the defect density for the hole-only device (Figure S20). It can be concluded that the 20% AABr treated film presented a lower V_{TFL} (0.84 V) than the control film (1.29 V), suggesting that the trap density in the perovskite film was reduced. More importantly, Figure 4g shows the average peak EQE derived from the EQE distribution (Figure 4f) as well as the PLQY for all quasi-2D PeLEDs with various AABr as a function of *RSO*. Coincidentally, the average EQE performance has an exponentially decreasing trend similar to PLQY. It clearly shows that the EL performance is strongly inversely dependent on the *RSO*, which means that the 20% AABr perovskite film has the lowest RSO, whereas the EQE performance is the most satisfying. This finding further confirms our previous conjecture. Thus, strengthening organic disorder ensures strong excitonic behavior, which is crucial for efficient PeLEDs.

Moreover, since the excess organic cations would reduce defects due to the suppressed crystallization of Pb[58], we compare the emission performance with different compositions, named (PEA:Pb = 1.2:1, and PEA+AA:Pb=1.2:1) to exclude the defect passivation. We found that the PEA:Pb=1.2 perovskite films also exhibited a slight luminescence enhancement benefiting from the defect passivation, as shown in Figure S21, whereas the (PEA+AA):Pb=1.2:1 sample shows a significant improvement. Therefore, we further believe the conformational modulation by AABr will play the main role in improving emission properties rather than the defect passivation caused by more organic spacers.

Discussion

In summary, we successfully controlled the structural disorder of organic cations in quasi-2D perovskites by incorporating AABr additives into quasi-2D phenyl-based

perovskites and determined this structural disorder by using sum-frequency generation vibrational spectroscopy (SFG-VS). We have revealed the critical role of molecular conformation in the excitonic behavior and derived the structure-property-performance relationships among relative structure ordering, radiative recombination, and EL emission efficiency. Such relationships confirmed that the PLQY and EQE show a robust inverse dependence on the molecular conformation order of the phenyl ring. Namely, the perovskite film with organic cation disorder yields a strong excitonic behavior. Theoretically and experimentally comparing the photophysical properties, the variation in stacking arrangement affects the mismatch of dielectric constants between the organic layer and inorganic framework, thus increasing the binding energy E_b and facilitating radiative recombination. As a result, our blue PeLEDs show a high EQE of 14.42% and prolonged spectral stability in open air with encapsulation. Our findings provide a broad avenue to explore the potential of organic spacer molecular conformation regulation for improving perovskite device performance.

Materials and Methods

Chemicals: CsBr, $PbBr_2$, $PbCl_2$, and PEABr were purchased from Xi'an Polymer Technology Corp. 2,2',2"-(1,3,5-Benzinetriyl)-tris(1-phenyl-1-H-benzimidalzole) (TBPi), PVK and lithium fluoride (LiF) were purchased from Lumtec. Acetamidinium bromide (AABr) was purchased from Greatcell Solar. PEDOT:PSS (AI 4083) was purchased from Heraeus. Ethyl acetate was purchased from Sigma-Aldrich. All materials were used as received.

Perovskite precursor solutions: The perovskite precursor solution was prepared by dissolving at an appropriate molar ratio of CsBr:$PbBr_2$:$PbCl_2$:PEABr = 1:0.6:0.4:1 in DMSO under continuous stirring for 4 h at room temperature, keeping the molar concentration of CsBr at 0.2 M. An additional x% AABr was introduced into the above precursor to obtain the molar ratio between AABr and CsBr (i.e., n_{AABr}/n_{CsBr} = x%).

Fabrication of blue PeLEDs: ITO glass substrates were ultrasonically washed in detergent solution, deionized water, acetone, and isopropanol for 15 mins and further treated with oxygen plasma for 20 mins. Then, the PEDOT:PSS was spin-cast onto the cleaned ITO-coated glass substrate at 4500 rpm for 45 s, followed by annealing at 140 ℃ for 20 mins. After that, 6 mg mL^{-1} PVK in chlorobenzene solution was spin-coated at 4000 rpm for 30 s and then annealed at 120 ℃ for 40 mins. The perovskite films were deposited in a glovebox filled with N_2 by spin-coating the precursor solution at 4500 rpm. for 55 s. Ethyl acetate was dropped at ~30 s after the beginning of the rotation. After that, a 40 nm thickness of TPBi and 1 nm LiF were deposited through shadow masks under a high vacuum. Finally, a 120 nm Al electrode was deposited as the cathode.

Characterization: XRD patterns were collected on a Bruker D8 Advance with Cu K radiation as the X-ray source at a scanning rate of 6° min^{-1}. UV-vis spectra were recorded on a Perkin Elmer Lambda 950 UV-Vis-NIR spectrometer. The photoluminescence spectra (PL) were measured using an Edinburgh Photoluminescence FLS 920. Time-resolved photoluminescence (TRPL) was collected using time-correlated single-photon counting for 10000 counts. Excitation was

provided by an Edinburgh EPL-375 nanosecond pulsed diode laser. The morphology was measured from field scanning electron microscopy (FESEM) images obtained from TESCAN MAIA3. The grazing-incidence wide-angle X-ray scattering (GIWAXS) data were obtained at beamline BL14B1 of the Shanghai Synchrotron Radiation Facility (SSRF), China. A monochromatic beam of λ=0.6887 Å was used, and the incident angle was 0.1°. All SFG-VS measurements were carried out by a femtosecond broadband sum frequency generation vibrational spectroscopy (SFG-VS) system. X-ray photoelectron spectroscopy (XPS) and ultraviolet photoelectron spectroscopy (UPS) spectra were obtained using a Thermo Fisher Nexsa XPS/UPS system.

Transient Absorption Spectroscopy: Transient absorption measurements were performed using a Helios setup. The transient dynamics in the fs-ns time region (50 fs - 7 ns) were acquired by Helios, which works in a nondegenerate pump-probe configuration. The pump pulses were generated from an optical parametric amplifier (OPerA Solo) pumped by a 1-kHz regenerative amplifier (Coherent Libra, 800 nm, 50 fs, 4 mJ). A mode lock Ti-sapphire oscillator (Coherent Vitesse, 100 fs, 80 MHz) was used to seed the amplifier. The probe pulse was a white light continuum generated by passing 800 nm fs pulses through a CaF_2 plate for the UV-visible part (250-650 nm).

PeLED characterization: A Keithley 2400 source meter, fiber integration sphere (FOIS-1), and QE Pro spectrometer (Ocean Optics) were utilized. The absolute radiance was calibrated by a standard Vis-NIR light source (HL-3P-INT-CAL plus, Ocean Optics). The EQE and spectral evolution with time were measured using the same system. All devices were encapsulated in a glovebox filled with N_2 and then characterized under an ambient atmosphere (60% relative humidity).

Acknowledgments

We wish to acknowledge the staff of beamlines at SSRF for providing the beam time. This work was financially supported by the Hong Kong Polytechnic University grant (1-CD7U); the National Natural Science Foundation of China (21925302, 22373081); the Innovation Program for Quantum Science and Technology (2021ZD0303303); the

Strategic Priority Research Program of the Chinese Academy of Sciences (XDB0450202); Hong Kong Innovation and Technology Fund (ITS/064/22); and Research Grants Council of Hong Kong (Project No. PolyU 25301522, PolyU 15301323, PolyU 25305222 and PolyU 15305221).

Author contributions

S.L. and S.Y. conceived the idea and supervised the project. L.Z., C.L. and Q.W. contributed equally. L.Z. carried out the materials synthesis, structural characterizations, device fabrications, and data analysis. C.L. and R.Z. performed SFG-VS and data analysis. Q.W. and H.R. conducted ultrafast transient absorption measurements and data analysis. F.S. carried out the XRD measurements. L.K., M.L., S.Y. and S.L. provided insightful discussions, and participated in data analysis and manuscript preparation. All authors discussed the results and revised the manuscript.

Competing interests

The authors declare no competing interests.

Supporting Information

Supporting Information is available from the Wiley Online Library or from the author.

Keywords

quasi-2D perovskite, conformation disorder, PeLEDs, dielectric constant, organic cation

Received: ((will be filled in by the editorial staff))

Revised: ((will be filled in by the editorial staff))

Published online: ((will be filled in by the editorial staff))

Reference

[1] K. Wang, Z. Y. Lin, Z. Zhang, L. Jin, K. Ma, A. H. Coffey, H. R. Atapattu, Y. Gao, J. Y. Park, Z. Wei, B. P. Finkenauer, C. Zhu, X. Meng, S. N. Chowdhury, Z. Chen, T. Terlier, T. H. Do, Y. Yao, K. R. Graham, A. Boltasseva, T. F. Guo, L. Huang, H. Gao, B. M. Savoie, L. Dou, *Nat. Commun.* **2023**, 14, 397.

[2] Z. Chu, W. Zhang, J. Jiang, Z. Qu, F. Ma, Y. Zhao, X. Chu, Y. Shen, Y. Li, Z. Yin, X. Zhang, J. You, *Nat. Electron.* **2023**, 6, 360.

[3] L. Zhang, C. Sun, T. He, Y. Jiang, J. Wei, Y. Huang, M. Yuan, *Light: Sci. Appl.* **2021**, 10, 61.

[4] L. Zhuang, Q. Wei, C. Li, H. Ren, Y. Li, F. Shi, L. Zhai, K. Leng, M. Li, S. P. Lau, *Adv. Opt. Mater.* **2022**, 10, 2201180.

[5] F. Zhang, D. H. Kim, H. Lu, J.-S. Park, B. W. Larson, J. Hu, L. Gao, C. Xiao, O. G. Reid, X. Chen, Q. Zhao, P. F. Ndione, J. J. Berry, W. You, A. Walsh, M. C. Beard, K. Zhu, *J. Am. Chem. Soc.* **2019**, 141, 5972-5979.

[6] C. Li, J. Yang, F. Su, J. Tan, Y. Luo, S. Ye, *Nat. Commun.* **2020**, 11, 5481.

[7] C. Li, R. Zhu, Z. Yang, J. Lai, J. Tan, Y. Luo, S. Ye, *Angew. Chem. Int. Edit.* **2022**, e202214208.

[8] M. Ban, Y. Zou, J. P. H. Rivett, Y. Yang, T. H. Thomas, Y. Tan, T. Song, X. Gao, D. Credgington, F. Deschler, H. Sirringhaus, B. Sun, *Nat. Commun.* **2018**, 9, 3892.

[9] C. Li, K. P. Loh, K. Leng, *Matter* **2022**, 5, 4153-4169.

[10] H. Cho, S.-H. Jeong, M.-H. Park, Y.-H. Kim, C. Wolf, C.-L. Lee, J. H. Heo, A. Sadhanala, N. Myoung, S. Yoo, S. H. Im, R. H. Friend, T.-W. Lee, *Science* **2015**, 350, 1222-1225.

[11] T.-H. Han, K. Y. Jang, Y. Dong, R. H. Friend, E. H. Sargent, T.-W. Lee, *Nature Reviews Materials* **2022**, 7, 757-777.

[12] Z. Ren, L. Li, J. Yu, R. Ma, X. Xiao, R. Chen, K. Wang, X. W. Sun, W.-J. Yin, W. C. H. Choy, *ACS Energy Lett.* **2020**, 5, 2569-2579.

[13] J. Hu, I. W. H. Oswald, S. J. Stuard, M. M. Nahid, N. Zhou, O. F. Williams, Z. Guo, L. Yan, H. Hu, Z. Chen, X. Xiao, Y. Lin, Z. Yang, J. Huang, A. M. Moran, H. Ade, J. R. Neilson, W. You, *Nat. Commun.* **2019**, 10, 1276.

[14] W. Sung, C. Müller, S. Hietzschold, R. Lovrinčić, N. P. Gallop, A. A. Bakulin, S. Nihonyanagi, T. Tahara, *Mater. Horiz.* **2020**, 7, 1348-1357.

[15] C. Li, R. Zhu, J. Lai, J. Tan, Y. Luo, S. Ye, *J. Phys. Chem. Lett.* **2021**, 12, 11817-11823.

[16] J. Lai, R. Zhu, J. Tan, Z. Yang, S. Ye, *Small* **2023**, 2303449.

[17] M. Zhang, Q. Chen, R. Xue, Y. Zhan, C. Wang, J. Lai, J. Yang, H. Lin, J. Yao, Y. Li, L. Chen, Y. Li, *Nat. Commun.* **2019**, 10, 4593.

[18] H. Chen, Q. Cheng, H. Liu, S. Cheng, S. Wang, W. Chen, Y. Shen, X. Li, H. Yang, H. Yang, J. Xi, Z. Chen, X. Lu, H. Lin, Y. Li, Y. Li, *Sci. Bull.* **2022**, 67, 1243-1252.

[19] R. Zhu, Q. Pei, J. Tan, X. Zheng, S. Ye, *Chinese J. Chem. Phys.* **2022**, 35, 738-746.

[20] K. S. Gautam, A. D. Schwab, A. Dhinojwala, D. Zhang, S. M. Dougal, M. S. Yeganeh, *Phys. Rev. Lett.* **2000**, 85, 3854-3857.
[21] Z. L. Wang, R. P. Gao, W. A. de Heer, P. Poncharal, *Appl. Phys. Lett.* **2002**, 80, 856-858.
[22] X. Lu, S. A. Spanninga, C. B. Kristalyn, Z. Chen, *Langmuir* **2010**, 26, 14231-14235.
[23] A. D. Curtis, A. R. Calchera, M. C. Asplund, J. E. Patterson, *Vib. Spectrosc.* **2013**, 68, 71-81.
[24] F. Vidal, A. Tadjeddine, *Rep. Prog. Phys.* **2005**, 68, 1095.
[25] Y. R. Shen, Fundamentals of Sum-Frequency Spectroscopy, Cambridge University Press, Cambridge, **2016**.
[26] H. Pashaei Adl, S. Gorji, G. Muñoz-Matutano, R. I. Sánchez-Alarcón, R. Abargues, A. F. Gualdrón-Reyes, I. Mora-Seró, J. P. Martínez-Pastor, *J. Lumin.* **2021**, 240, 118453.
[27] J.-H. Xie, Q.-L. Zhou, Accounts of Chemical Research 2008, 41, 581-593.
[28] A. P. Alivisatos, *Science* **1996**, 271, 933-937.
[29] J. Wang, Z. Paszti, M. A. Even, Z. Chen, *J. Am. Chem. Soc.* **2002**, 124, 7016-7023.
[30] X. Gong, O. Voznyy, A. Jain, W. Liu, R. Sabatini, Z. Piontkowski, G. Walters, G. Bappi, S. Nokhrin, O. Bushuyev, M. Yuan, R. Comin, D. McCamant, S. O. Kelley, E. H. Sargent, *Nat. Mater.* **2018**, 17, 550-556.
[31] X. Hong, T. Ishihara, A. V. Nurmikko, *Phys. Rev. B.* **1992**, 45, 6961-6964.
[32] J. T. Lin, C. C. Liao, C. S. Hsu, D. G. Chen, H. M. Chen, M. K. Tsai, P. T. Chou, C. W. Chiu, *J. Am. Chem. Soc.* **2019**, 141, 10324-10330.
[33] P. Li, H. Dong, J. Xu, J. Chen, B. Jiao, X. Hou, J. Li, Z. Wu, *ACS Energy Lett.* **2020**, 5, 2327-2334.
[34] P. Singh, R. Mukherjee, S. Avasthi, *ACS Appl. Mater. Interfaces* **2020**, 12, 13982-13987.
[35] Y. Jiang, M. Cui, S. Li, C. Sun, Y. Huang, J. Wei, L. Zhang, M. Lv, C. Qin, Y. Liu, M. Yuan, *Nat. Commun.* **2021**, 12, 336.
[36] I. Anusca, S. Balčiūnas, P. Gemeiner, Š. Svirskas, M. Sanlialp, G. Lackner, C. Fettkenhauer, J. Belovickis, V. Samulionis, M. Ivanov, B. Dkhil, J. Banys, V. V. Shvartsman, D. C. Lupascu, *Adv. Energy Mater.* **2017**, 7, 1700600.
[37] H. Takagi, H. Kunugita, K. Ema, *Phys. Rev. B* **2013**, 87.
[38] X.-K. Liu, W. Xu, S. Bai, Y. Jin, J. Wang, R. H. Friend, F. Gao, *Nat. Mater.* **2021**, 20, 10-21.
[39] G. Zheng, C. Zhu, J. Ma, X. Zhang, G. Tang, R. Li, Y. Chen, L. Li, J. Hu, J. Hong, Q. Chen, X. Gao, H. Zhou, *Nat. Commun.* **2018**, 9, 2793.
[40] J. Wang, S. Luo, Y. Lin, Y. Chen, Y. Deng, Z. Li, K. Meng, G. Chen, T. Huang, S. Xiao, H. Huang, C. Zhou, L. Ding, J. He, J. Huang, Y. Yuan, *Nat. Commun.* **2020**, 11, 582.
[41] A. Z. Chen, M. Shiu, J. H. Ma, M. R. Alpert, D. Zhang, B. J. Foley, D.-M. Smilgies, S.-H. Lee, J. J. Choi, *Nat. Commun.* **2018**, 9, 1336.
[42] G. Xing, B. Wu, X. Wu, M. Li, B. Du, Q. Wei, J. Guo, E. K. L. Yeow, T. C. Sum,

W. Huang, *Nat. Commun.* **2017**, 8, 14558.
[43] Z. Gan, Y. Cheng, W. Chen, K. P. Loh, B. Jia, X. Wen, *Adv. Sci.* **2021**, 8, 2001843.
[44] Z. Gan, W. Chen, C. Liu, J. Zhang, Y. Di, L. Yu, L. Dong, B. Jia, X. Wen, *Adv. Photon. Res.* **2022**, 3, 2100283.
[45] Y. Jiang, J. Wei, M. Yuan, *J. Phys. Chem. Lett.* **2021**, 12, 2593-2606.
[46] M. Yuan, L. N. Quan, R. Comin, G. Walters, R. Sabatini, O. Voznyy, S. Hoogland, Y. Zhao, E. M. Beauregard, P. Kanjanaboos, Z. Lu, D. H. Kim, E. H. Sargent, *Nat. Nanotechnol.* **2016**, 11, 872-877.
[47] Q. Zhang, E. Linardy, X. Wang, G. Eda, *ACS Nano* **2020**, 14, 11482-11489.
[48] S. Panuganti, L. V. Besteiro, E. S. Vasileiadou, J. M. Hoffman, A. O. Govorov, S. K. Gray, M. G. Kanatzidis, R. D. Schaller, *J. Am. Chem. Soc.* **2021**, 143, 4244-4252.
[49] P. Chen, Y. Meng, M. Ahmadi, Q. Peng, C. Gao, L. Xu, M. Shao, Z. Xiong, B. Hu, *Nano Energy* **2018**, 50, 615-622.
[50] W. Zhou, Y. Shen, L. X. Cao, Y. Lu, Y. Y. Tang, K. Zhang, H. Ren, F. M. Xie, Y. Q. Li, J. X. Tang, *Adv. Funct. Mater.* **2023**, 33, 2301425.
[51] Y. Jiang, C. Qin, M. Cui, T. He, K. Liu, Y. Huang, M. Luo, L. Zhang, H. Xu, S. Li, J. Wei, Z. Liu, H. Wang, G.-H. Kim, M. Yuan, J. Chen, *Nat. Commun.* **2019**, 10, 1868.
[52] Y.-H. Niu, M. S. Liu, J.-W. Ka, A. K.-Y. Jen, *Appl. Phys. Lett.* **2006**, 88.
[53] M. Karlsson, Z. Yi, S. Reichert, X. Luo, W. Lin, Z. Zhang, C. Bao, R. Zhang, S. Bai, G. Zheng, P. Teng, L. Duan, Y. Lu, K. Zheng, T. Pullerits, C. Deibel, W. Xu, R. Friend, F. Gao, *Nat. Commun.* **2021**, 12, 361.
[54] L. Zhang, Y. Jiang, Y. Feng, M. Cui, S. Li, X. Fu, H. Y. Hsu, C. Qin, M. Yuan, *Angew. Chem. Int. Edit.* **2023**, e202302184.
[55] W. Xu, Q. Hu, S. Bai, C. Bao, Y. Miao, Z. Yuan, T. Borzda, A. J. Barker, E. Tyukalova, Z. Hu, M. Kawecki, H. Wang, Z. Yan, X. Liu, X. Shi, K. Uvdal, M. Fahlman, W. Zhang, M. Duchamp, J.-M. Liu, A. Petrozza, J. Wang, L.-M. Liu, W. Huang, F. Gao, *Nat. Photonics* **2019**, 13, 418-424.
[56] M. Abdi-Jalebi, Z. Andaji-Garmaroudi, S. Cacovich, C. Stavrakas, B. Philippe, J. M. Richter, M. Alsari, E. P. Booker, E. M. Hutter, A. J. Pearson, S. Lilliu, T. J. Savenije, H. Rensmo, G. Divitini, C. Ducati, R. H. Friend, S. D. Stranks, *Nature* **2018**, 555, 497-501.
[57] X. Xiao, J. Dai, Y. Fang, J. Zhao, X. Zheng, S. Tang, P. N. Rudd, X. C. Zeng, J. Huang, *ACS Energy Lett.* **2018**, 3, 684-688.
[58] Y. Han, S. Park, C. Kim, M. Lee, I. Hwang, *Nanoscale* **2019**, 11, 3546.

Entry for the Table of Contents

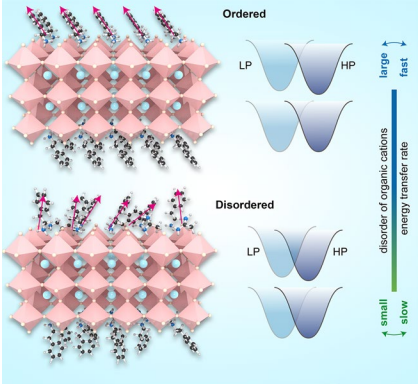

The disorder of organic cation is usually perceived as detrimental to device performance, scarfing the charge carrier mobility. Here, we control and quantify the precise manipulation of conformational disorder among quasi-2D perovskite, suggesting that the increasing disorder enhances excitonic behaviour, which is promising for high-performance PeLED devices.